

# Investigation of in-plane nuclear field formation in single self-assembled quantum dots

S. Yamamoto,<sup>1</sup> R. Matsusaki,<sup>1</sup> R. Kaji,<sup>1</sup> and S. Adachi<sup>1,\*</sup>

<sup>1</sup>*Division of Applied Physics, Hokkaido University, N13 W8, Kitaku, Sapporo 060-8628, Japan*

(Dated: April 6, 2024)

We studied the formation mechanism of the in-plane nuclear field in single self-assembled  $\text{In}_{0.75}\text{Al}_{0.25}\text{As}/\text{Al}_{0.3}\text{Ga}_{0.7}\text{As}$  quantum dots. The Hanle curves with an anomalously large width and hysteretic behavior at the critical transverse magnetic field were observed in many single quantum dots grown in the same QD sample. In order to explain the anomalies in the Hanle curve indicating the formation of a large nuclear field perpendicular to the photo-injected electron spin polarization, we propose a new model based on the current phenomenological model for dynamic nuclear spin polarization. The model includes the effects of the nuclear quadrupole interaction and the sign inversion between in-plane and out-of-plane g-factors, and the model calculations reproduce successfully the characteristics of the observed anomalies in the Hanle curves.

PACS numbers: 73.21.La, 78.67.Hc, 71.35.Pq, 71.70.Jp

## I. INTRODUCTION

The study of nuclear spin physics in semiconductor quantum dots (QDs) is an active research field currently. This is because the role of hyperfine interaction (HFI), which is the magnetic interaction between a localized electron and the lattice nuclei, is drastically enhanced in QD structures compared with those in bulks and quantum wells due to a strong localization of the electron wave function [1–3]. Since it is possible to transfer the angular momentum from light onto nuclei via electron spin, a macroscopic nuclear spin polarization (NSP) which is orders of magnitude larger than the value in thermal equilibrium can be generated actually at cryogenic temperatures, and in turn, the resultant nuclear field (Overhauser field,  $B_n$ ) up to a few Teslas affects the electron spin dynamics significantly [4–10]. Because the lattice nuclei act as a reservoir for an optically or electrically injected electron spin, the *engineering* of nuclear spins such as the optical manipulation of the NSP not only leads to the potential applications but also opens up a new spin physics.

The dynamics of NSP is determined by the environment which the nuclei are exposed to, such as presences of an external magnetic field and/or an unpaired electron in a QD, and dipole-dipole interaction among the neighbor nuclei. In particular, nuclear quadrupole interaction (QI), which originates from the coupling of a nuclear spin with  $I > 1/2$  to the electric field gradients (EFG) [11], has received a lot of attention recently. Since the lattice strain is used as a driving force for the spontaneous formation process of self-assembled QDs (SA-QDs), the residual strain and the resultant large EFG arise in these QDs. Therefore, the impact of QI is expected to gain considerably and to play key roles for various novel phenomena observed in SA-QDs [12–15]. The QI yields the non-equivalent energy splitting depending on the value  $|I_{z'}|$ , where  $z'$ -axis is the quantization axis determined by EFG and is found to be usually close to the sample growth axis ( $z$ -axis) in the SA-QDs [16, 17]. Then, QI can be treated as an effective field affecting the nuclear spins, the quadrupolar field,

and it stabilizes the NSP in  $z'$ -axis as reported in ensembles of SA-InP/InGaP QDs [18] and single SA-InAs/GaAs QDs [19].

Recently, the formation of in-plane nuclear field was reported in single SA-InAs/GaAs QDs under quasisresonant excitation by Krebs et al. [15] and nonresonant excitation by Nilsson et al. [20], and it seemed to be related also to QI. The in-plane nuclear field was detected by observing the electron spin depolarization curve in Voigt configuration (i.e. Hanle curve). In their pioneering works, the Hanle curve was distorted drastically from a normal Lorentzian shape in the following respects: a  $\sim 20$  times larger width than the one expected from the electron spin lifetime, and the abrupt change in the degree of circular polarization (DCP), and thus, the anomalous Hanle curve has a shape like a circus tent. In addition, the fact that such anomalies in Hanle curve have not been observed in single droplet GaAs QDs [21] which is free from internal strain suggests that the QI contributes significantly to an anomalous Hanle curve observed in SA-QDs. However, the origin of the anomalies in the Hanle curves has not been revealed entirely. The knowledge of the in-plane nuclear field formation may lead directly to an optical control of the nuclear field direction, and therefore, it is very important.

In this work, we study the formation mechanism of the in-plane nuclear field via the Hanle effect measurements and model calculations. The anomalously distorted Hanle curves similar to Ref. 15 are observed in single InAlAs QDs, and we show that the anomalies of the Hanle curves can be reproduced qualitatively by a proposed model including the QI and the sign inversion of g-factors.

## II. QD SAMPLE AND ANOMALOUS HANLE CURVES

SA- $\text{In}_{0.75}\text{Al}_{0.25}\text{As}/\text{Al}_{0.3}\text{Ga}_{0.7}\text{As}$  QDs grown on (100)-GaAs substrate by molecular beam epitaxy were used in this study. The QDs have a lens-shaped profile, and the typical diameter and height were evaluated to be  $\sim 20$  nm and  $\sim 4$  nm, respectively, by the atomic force microscopy measurements of a reference uncapped QD layer and the cross-section transmission electron microscope observation. After the fabrication of small mesa structures, the micro-photoluminescence (PL) measurements under the transverse magnetic fields ( $B_x$ ) up to

\* adachi-s@eng.hokudai.ac.jp

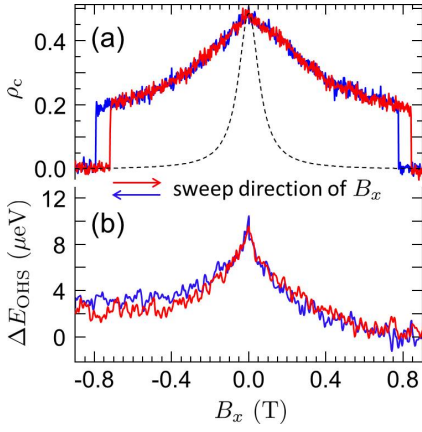


FIG. 1. (color online) (a) The anomalous Hanle curves observed in the SA-InAlAs QD. The red (blue) curve represents the DCP of  $X^+$  PL with increasing (decreasing)  $B_x$ . The dotted curve is the normal Hanle curve expected with typical values of spin lifetime and g-factor of electron. (b) The observed Overhauser shift as a function of  $B_x$ , which is used as a measure of  $|B_{n,z}|$ .

1 T were carried out at 6 K. The QD sample was excited by a cw Ti:sapphire laser tuned to  $\sim 730$  nm, which corresponds to the transition energy to the foot of the wetting layer of the QDs.

The polarization of an excitation beam was adjusted carefully to the circular polarization by a combination of a linear polarizer, a half wave plate, and a quarter wave plate (QWP). The circularly polarized ( $\sigma^+$ ,  $\sigma^-$ ) PL components were converted to the linearly polarized ones ( $\pi^x$ ,  $\pi^y$ ) by another QWP inserted into the detection path, and they were displaced spatially from each other by a beam displacer. Each displaced PL component was dispersed by a spectrometer and was focused on a different area of the Si-CCD detector. Therefore, the energy splitting between the  $\sigma^+$  and  $\sigma^-$  components and the DCP of the PL spectra can be acquired by a single exposure process. The details of the experimental apparatus is seen in Ref. 22. The energy resolution of our measurement system is  $\leq 5 \mu\text{eV}$  by spectral fitting.

In this work, we focus on the PL of positive trion ( $X^+$ ). The  $X^+$  ground state consists of two holes in a spin-singlet state and one electron, and thus, the DCP of this charge state is determined only by the electron spin right before radiative recombination. Here, the DCP is defined as  $\rho_c = (I^- - I^+) / (I^- + I^+)$ , where  $I^{+(-)}$  represents the integrated PL intensity of  $\sigma^{+(-)}$  component. The DCP is related directly to the projection of the averaged electron spin along the sample growth axis,  $\langle S_z \rangle$ , and the relation  $\langle S_z \rangle = \rho_c / 2$  is held for  $X^+$  case.

Figure 1(a) is an example of the anomalous Hanle curves observed in the SA-InAlAs QD sample. In the figure, the red (blue) curve represents the observed DCP with increasing (decreasing)  $B_x$  under  $\sigma^-$  excitation, while the dashed curve is an expected *normal* Hanle curve, which is free from the effect of  $B_n$  and has a Lorentzian shape with the full width  $2B_{1/2} (\sim 130 \text{ mT})$  [23]. As clearly shown, the observed curves

have quite larger widths than the expected one. Further, the DCP changes suddenly at the critical field  $|B_x^c| \sim 0.8 \text{ T}$ , and  $|B_x^c|$  is different depending on the sweep direction of  $B_x$  (i.e. a hysteretic behavior occurs). Such anomalous characters were observed in not only a specific QD but also all the QDs we measured in the same sample (not shown here). In the work by Krebs et al. [15], the Hanle curves with the similar anomalies were observed in single SA-InAs/GaAs QDs, where the bistable behavior of a nuclear field in  $x$ -direction  $B_{n,x}$  and a compensation of  $B_x$  by  $B_{n,x}$  were confirmed unambiguously.

The observed energy splittings between the  $\sigma^+$  and  $\sigma^-$  PL components are plotted in Fig. 1(b). Since the external magnetic field is applied in  $x$ - $y$  plane, the energy splitting detected in ( $\sigma^+$ ,  $\sigma^-$ ) basis is determined only by  $z$ -component of the nuclear field,  $B_{n,z}$ . Thus, we term the corresponding energy splitting the Overhauser shift,  $\Delta E_{\text{OHS}}$ . As seen in the figure, the maximal value of  $\Delta E_{\text{OHS}}$  of  $\sim 10 \mu\text{eV}$  appears at  $B_x = 0 \text{ T}$ , and it corresponds to the  $B_{n,z}$  of  $-0.5 \text{ T}$  by considering the relation  $B_{n,z} = \Delta E_{\text{OHS}} / (g_z^e \mu_B)$ , where  $g_z^e$  is the electron g-factor in  $z$ -direction and  $\mu_B$  is the Bohr magneton.  $\Delta E_{\text{OHS}}$  reduces gradually with increasing  $|B_x|$  and approaches almost zero around  $|B_x^c|$ . Further, the observed  $\Delta E_{\text{OHS}}$  is slightly asymmetric with respect to the sign in  $B_x$ .

The set of the electron g-factor of this single QD, ( $g_x^e$ ,  $g_y^e$ ,  $g_z^e$ ) is described in Appendix A, and it is required for the evaluation of the nuclear field and the model calculations in the next section.

### III. MODEL CALCULATIONS AND DISCUSSIONS

In this section, we propose a dynamics model of a coupled electron-nuclear spin system in order to reproduce the observed anomalous Hanle curves shown in the previous section.

The evolution of an electron spin polarization  $\langle S \rangle$  can be described by the Bloch equation:

$$\frac{d\langle S \rangle}{dt} = \frac{\bar{g}_e \mu_B}{\hbar} \mathbf{B}_T^{(e)} \times \langle S \rangle - \frac{\langle S \rangle - S_0}{T_s}, \quad (1)$$

where  $\bar{g}_e$  is the electron g-tensor,  $\mathbf{B}_T^{(e)}$  is an effective magnetic field seen by a QD electron, and  $S_0 = (0, 0, S_0)$  is the average electron spin polarization in the absence of  $\mathbf{B}_T^{(e)}$ . The first and the second terms in the right-hand side represent the Larmor precession and the electron spin relaxation with a characteristic time  $T_s$ , respectively. The steady state solution of Eq. (1) gives a Hanle curve according to the relation  $\rho_c = 2\langle S_z \rangle$  (see Appendix B). Since the nuclear field  $\mathbf{B}_n$  ( $\propto \langle I \rangle$ : NSP) as well as the externally applied field  $\mathbf{B}_{\text{ext}}$  contributes to  $\mathbf{B}_T^{(e)}$  ( $\equiv \mathbf{B}_{\text{ext}} + \mathbf{B}_n$ ), it is essential to consider the spin dynamics of nuclei. In this work, the external field is applied in the sample growth plane, and thus, it can be written as  $\mathbf{B}_{\text{ext}} = (B_x, 0, 0)$ .

As widely accepted, the contact-type HFI includes the flip-flop term between an electron and nuclear spins, i.e.,  $\propto (\hat{I}_+ \hat{S}_- + \hat{I}_- \hat{S}_+)$ , and it allows the spin transfer from the optically-injected electron to the lattice nuclei system [1]. The dynamics of the NSP component  $\langle I_k \rangle$  ( $k = x, y, z$ ) follows the

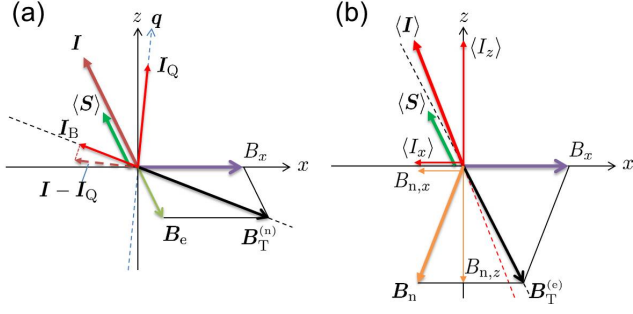


FIG. 2. (color online) Schematics of the spin polarizations and the resultant effective fields. (a) A portion of the HFI-induced  $\mathbf{I}$  is protected by QI and the other one is preserved by  $\mathbf{B}_T^{(n)}$ :  $\mathbf{I}_Q$  and  $\mathbf{I}_B$ . For generality, the vector  $\mathbf{q}$  is tilted slightly from  $z$ -axis. (b) The protected NSP  $\langle \mathbf{I} \rangle$  ( $= \mathbf{I}_Q + \mathbf{I}_B$ ) induces  $\mathbf{B}_n$  eventually. Since the sign inversion of  $g$ -tensor is assumed,  $B_{n,x}$  is depicted to be parallel to  $\langle I_x \rangle$  while  $B_{n,z}$  is anti-parallel to  $\langle I_z \rangle$ .

phenomenological equation [2, 3]:

$$\frac{d\langle I_k \rangle}{dt} = \frac{1}{T_{NF,k}} \left[ Q(\langle S_k \rangle - \langle S_k^{eq} \rangle) - \langle I_k \rangle \right] - \frac{1}{T_{ND,k}} \langle I_k \rangle, \quad (2)$$

where  $Q = \tilde{I}(\tilde{I} + 1)/[S(S + 1)]$  is a numerical constant of the momentum conversion,  $\langle S_k^{eq} \rangle$  is the electron spin polarization at thermal equilibrium, and  $1/T_{ND,k}$  is the relaxation rate of the NSP in  $k$ -direction. The NSP formation rate  $1/T_{NF,k}$  depends on the NSP itself, and it is given by

$$\frac{1}{T_{NF,k}} = 2f_e \tau_c \left( \frac{\tilde{A}_k}{N\hbar} \right)^2 \left\{ 1 + \left[ g_k^e \mu_B (B_{ext,k} + B_{n,k}) \tau_c / \hbar \right]^2 \right\}, \quad (3)$$

where  $f_e$  ( $0 \leq f_e \leq 1$ ) is a filling factor representing the occupation of a QD by an unpaired electron spin,  $\tau_c$  is a correlation time of HFI,  $N$  is the number of nuclei related to the interaction,  $\tilde{A}_k$  is the averaged coupling constant of HFI, and  $B_{n,k} = \tilde{A}_k I_k / (g_k^e \mu_B)$  is the  $k$ -component of the nuclear field, respectively. This spin dynamics model has achieved success to explain the experimental observations about  $\langle I_z \rangle$  and thus the behavior of  $B_{n,z}$  in the previous studies [6–10].

Moreover, it is necessary to consider the effective magnetic field experienced by nuclear spins,  $\mathbf{B}_T^{(n)}$  explicitly. As is the case with  $\mathbf{B}_T^{(e)}$ ,  $\mathbf{B}_T^{(n)}$  is determined by the sum of the external field and the Knight field  $\mathbf{B}_e$ , i.e.  $\mathbf{B}_{ext} + \mathbf{B}_e$ . Here,  $\mathbf{B}_e$  refers to the effective field caused by the electron spin polarization and is proportional to  $\langle \mathbf{S} \rangle$ . The introduction of  $\mathbf{B}_e$  explains the Lorentzian Hanle curve with W-shaped dip [1] which appears in a very low magnetic field region ( $B_{ext} \lesssim 0.1$  T) as shown later (Fig. 3(b)). However, it is not possible to describe the observed anomalous Hanle curves with a quite large width (e.g.,  $|B_x^c| \sim 0.8$  T in Fig. 1(a) and the results in Ref.15) in this framework. Therefore, we improve the conventional model by introducing the effects of QI.

One of the significant improvements is the NSP stabilization due to QI. Note that the HFI-induced NSP,  $\mathbf{I}$  must be collinear with the electron spin polarization according to

Eq. (2), and it evolves under the effect of  $\mathbf{B}_T^{(n)}$ . As depicted in Fig. 2(a), we assume that the NSP component along the principle axis of QI is preserved partially with a ratio  $r_Q$  ( $0 < r_Q \leq 1$ ). Hence the QI-preserving component  $\mathbf{I}_Q$  is given as

$$\mathbf{I}_Q = r_Q (\mathbf{I} \cdot \mathbf{q}) \mathbf{q}, \quad (4)$$

where  $\mathbf{q}$  is a unit vector along with the principle axis of QI. The other component (i.e.,  $\mathbf{I} - \mathbf{I}_Q$ ) is affected by the effective magnetic field, and its projection to  $\mathbf{B}_T^{(n)}$  termed as  $\mathbf{I}_B$  is also preserved as follows:

$$\mathbf{I}_B = \frac{(\mathbf{I} - \mathbf{I}_Q) \cdot \mathbf{B}_T^{(n)}}{|\mathbf{B}_T^{(n)}|} \frac{\mathbf{B}_T^{(n)}}{|\mathbf{B}_T^{(n)}|}. \quad (5)$$

Eventually, only the sum of  $\mathbf{I}_Q$  and  $\mathbf{I}_B$ ,  $\langle \mathbf{I} \rangle$  survives and acts as a nuclear field according to the following relation:

$$\mathbf{B}_n = \frac{\tilde{A}}{\bar{g}_e \mu_B} (\mathbf{I}_Q + \mathbf{I}_B). \quad (6)$$

It should be noted that the survived  $\langle \mathbf{I} \rangle$  is non-collinear with  $\langle \mathbf{S} \rangle$  and the original  $\mathbf{I}$  as shown in Fig. 2 (b).

In the following model calculations, we assume that the ratio  $r_Q$  in Eq. (4) depends on the applied transverse field as follows:

$$r_Q(B_x) = \frac{r_0}{1 + (B_x/B_Q)^2}, \quad (7)$$

where  $B_Q$  is a measure of the QI strength as converted to an effective magnetic field (quadrupolar field). Note that the quadrupolar field  $B_Q$  cannot induce the spin precession. The parameter  $r_0$  is an amplitude of the Lorentzian shape, and the condition  $r_0 = 1$  is used in the calculations. The efficiency of the NSP stabilization is supposed to decrease with increasing  $|B_x|$  if the principle axis of QI is almost perpendicular to  $B_x$ . This is because the relative strength of QI to  $B_x$  reduces with increasing  $|B_x|$  and the NSP component perpendicular to  $B_x$  is easy to relax. In our InAlAs QDs, the magnitude of the quadrupolar field is estimated to be  $\sim 280$  mT from other experiments [22].

Further, we assume an anisotropic nature in the nucleus *or* electron  $g$ -tensor, that is, the sign of the in-plane  $g$ -factor is opposite to that of  $z$ -component. Thus, in Fig. 2(b),  $B_{n,x}$  is depicted to be parallel to  $\langle I_x \rangle$  while  $B_{n,z}$  is anti-parallel to  $\langle I_z \rangle$ . Because  $B_{n,k}$  includes the HFI coupling constant  $\tilde{A}_k$  and  $g_k^e$ , the direction of the resultant  $B_{n,k}$  is determined by the signs of  $g_k^n$  and  $g_k^e$ . The sign inversion of  $g$ -factors in the in-plane and out-of-plane is required to achieve the compensation of the external field  $B_x$  by in-plane nuclear field  $B_{n,x}$  that increases by a flip-flop term of HFI.

Figure 3 highlights the impacts of the NSP stabilization and the sign inversion of  $g$ -factors. In this framework, the calculated results can be classified by two important parameters: the sign of  $g_{x(y)}^e \cdot g_z^e$  (or  $g_{x(y)}^n \cdot g_z^n$ ) and  $r_Q$  in Eq. (4). The latter represents the presence or absence of  $\mathbf{I}_Q$ . In Fig. 3, we set  $g_z^e < 0$  and the nucleus  $g$ -factors  $g_k^n$  are assumed to be isotropic. In the figure, (a)  $r_Q \neq 0$ ,  $g_x^e > 0$ , (b)  $r_Q = 0$ ,  $g_x^e > 0$ ,

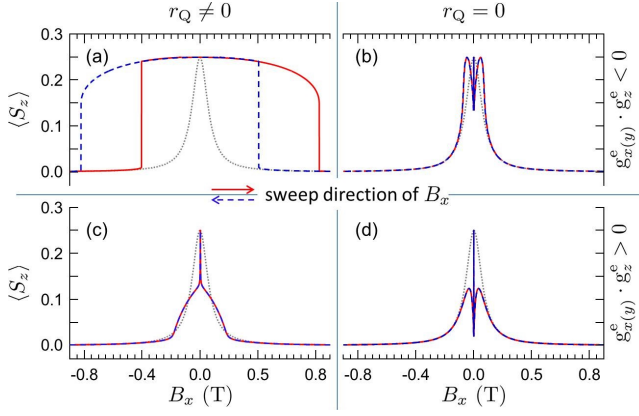


FIG. 3. (color online) The typical calculated  $\langle S_z \rangle$  depending on QI and the sign of  $g_x^e$ . Here  $g_z^e$  is set to be negative ( $g_z^e < 0$ ). (a)  $r_Q \neq 0$ ,  $g_x^e > 0$ , (b)  $r_Q = 0$ ,  $g_x^e > 0$ , (c)  $r_Q \neq 0$ ,  $g_x^e < 0$ , (d)  $r_Q = 0$ ,  $g_x^e < 0$ .  $g_k^n$  is assumed to be isotropic for  $k = x, y, z$ . Other parameters are same in all cases. In the case of  $r_Q \neq 0$ ,  $\mathbf{q}$  is set along  $z$ -axis. The dotted gray line represents a Lorentzian Hanle curve with the typical InAlAs QD parameters. [23]

(c)  $r_Q \neq 0$ ,  $g_x^e < 0$ , (d)  $r_Q = 0$ ,  $g_x^e < 0$ , and all the other parameters are identical in (a)-(d) [24]. In the calculations, the relaxation time of the NSP  $T_{ND,k}$  is assumed to be isotropic.

In the cases of  $r_Q=0$  ((b) and (d)), the effect of a tilting  $\mathbf{B}_n$  is reproduced as discussed in Ref. 1.  $\mathbf{B}_n$  cooled by  $\mathbf{B}_e$  inclines by the applied  $B_x$ . The W-shaped dip (i.e. recovery of DCP) in (b) may correspond to the actual observations in AlGaAs bulks [1] and single droplet GaAs/AlGaAs QDs [21]. Since an emerged  $B_{n,x}$  by tilting of  $\mathbf{B}_n$  is small and nearly constant, the compensation (b) or enhancement (d) of  $B_x$  by  $B_{n,x}$  occurs within a low  $B_x$  region ( $\leq 0.1$  T), and therefore, the depolarization is converging quickly to the tails of a normal Lorentzian curve regardless of a sweep direction of  $B_x$ .

In the case of (a) ( $r_Q \neq 0$  and  $g_x^e \cdot g_z^e < 0$ ), the Hanle curves indicates a much larger full width than  $2B_{1/2}$ . The extension of the width is induced by the compensation of  $B_x$  by  $B_{n,x}$  that follows the change in  $B_x$ , and therefore, the bistable (hysteretic) behavior appears. On the other hand, the effect of  $r_Q \neq 0$  is strongly reduced in (c) since  $B_{n,x}$  enhances the total effective field and the growth of  $B_{n,x}$  is terminated by high energy cost in the flip-flop process. Therefore, only slight broadening of the curve occurs.

Figure 4 (a) shows the calculated results about the components of  $\langle \mathbf{S} \rangle$  and  $\mathbf{B}_n$  under the condition corresponding to the case of Fig. 3 (a). However, in Fig. 4, the sign inversion is present in nucleus g-factors (i.e.  $g_x^n \cdot g_z^n < 0$ ) and both conditions of g-factors (Figs. 3 and 4) give the same results basically [25]. In the figure,  $\langle S_y \rangle$  and  $B_{n,y}$  are not shown for an easy view because of their small magnitudes within  $|B_x| < |B_x^c|$ .

The calculations reproduce well the experimental results in Fig. 1 at the following characteristic points;

1. a large value of  $\langle S_z \rangle$  is preserved even under a large  $|B_x|$  until the critical field  $B_x^c$ ,

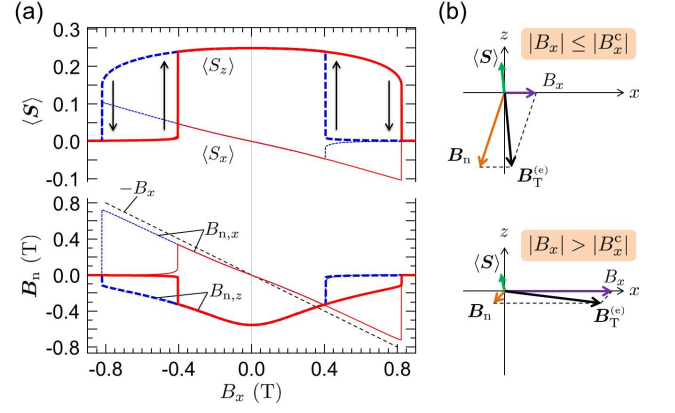


FIG. 4. (color online) (a) The calculated  $\langle S_z \rangle$  (thick lines) and  $\langle S_x \rangle$  (thin lines) in upper panel, and  $B_{n,z}$  (thick lines) and  $B_{n,x}$  (thin lines) in lower panel under the condition,  $r_Q \neq 0$  and  $g_x^n \cdot g_z^n < 0$ . The solid (dashed) lines represent the results with increasing (decreasing)  $B_x$ .  $\langle S_y \rangle$  and  $B_{n,y}$  are not shown here for an easy view. [24] (b) Schematics of  $\langle \mathbf{S} \rangle$  and  $\mathbf{B}_n$  in  $xz$ -plane corresponding to the case  $|B_x| \leq |B_x^c|$  (upper panel) and  $|B_x| > |B_x^c|$  (lower panel).

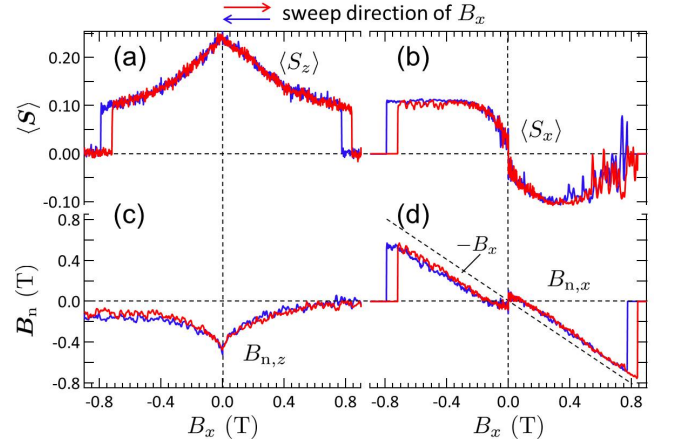


FIG. 5. (color online) (a) The observed  $\langle S_z \rangle (= \rho_c/2)$ , (b) the expected  $\langle S_x \rangle$ , (c) the observed  $B_{n,z}$ , and (d) the expected  $B_{n,x}$ . Red (blue) line represents the result with increasing (decreasing)  $B_x$ . (b) and (d) are obtained by substituting the observed  $\langle S_z \rangle$  and  $B_{n,z}$  into Eqs. (B2) and (B3).

2.  $\langle S_z \rangle$  changes abruptly at  $B_x^c$  and shows the hysteretic (thus, bistable) behavior,
3.  $\langle S_z \rangle$ -curve is symmetric with respect to the sweep direction of  $B_x$ ,
4.  $|B_{n,z}|$  reduces gradually with increasing  $|B_x|$ .

The schematics of the electron spin polarization and the nuclear field are summarized in Fig. 4 (b); the upper (lower) panel corresponds to the case  $|B_x| \leq |B_x^c|$  ( $|B_x| > |B_x^c|$ ). In the small- $B_x$  region, the in-plane component of  $\mathbf{B}_n$  compensates the applied field, and the effective field  $\mathbf{B}_T^{(e)}$  is almost parallel

to  $z$ -direction. Therefore, a large value of  $\langle S_z \rangle$  is kept under the condition  $|B_x| \leq |B_x^c|$ . In the large- $B_x$  region, on the other hand, since the induced  $B_n$  is quite small, the vector  $\langle S \rangle$  feels a large transverse field and  $\langle S_z \rangle$  relaxes quickly.

Note that the  $B_x$ -dependence of  $r_Q$  (as shown in Eq. (7)) is necessary to reproduce the gradual reduction in  $B_{n,z}$ ; if  $r_Q$  is independent of  $B_x$  and has a constant value, the calculated  $B_{n,z}$  shows a similar shape with  $\langle S_z \rangle$  and abrupt changes occur at  $|B_x^c|$  [27]. Further, a tilting angle of  $\mathbf{q}$  from the  $z$ -direction induces the asymmetry and horizontal shift of the Hanle curve.

Finally, we provide the  $B_x$ -dependence of  $\langle S_x \rangle$  and  $B_{n,x}$  expected from experimental data of  $\langle S_z \rangle$  and  $B_{n,z}$  in Fig. 5. They are obtained from the steady state solutions of the Bloch equation (see Appendix B) by substituting the observed  $\langle S_z \rangle = \rho_c/2$  and  $B_{n,z} = \Delta E_{\text{OHS}}/(g_z^e \mu_B)$  and solving for  $\langle S_x \rangle$  and  $B_{n,x}$ . Comparing the expected  $|\langle S_x \rangle|$  (Fig. 5 (b)) with the computed  $|\langle S_x \rangle|$  (Fig. 4 (a)), the expected one has the maximal value and shows saturation or decay while the computed  $|\langle S_x \rangle|$  increases monotonically with increasing  $|B_x|$ . Asymmetry in the expected  $|\langle S_x \rangle|$  with respect to  $B_x$  is originated from the asymmetry of  $B_{n,z}$ , which has small but finite value in a large negative  $B_x$  region.

As a whole, the proposed model can reproduce the observed results qualitatively. However, the quantitative disagreement of the hysteresis width of  $|B_x^c|$  between the calculated and observed results could not be resolved at present in the range of the parameters we changed. Despite such a disagreement,  $|B_x^n|$  agrees well with the computed results. These suggest that there is a possibility that another mechanism for the in-plane nuclear field formation may work in a relatively large  $|B_x|$  region. One plausible candidate is a non-collinear HFI process [28], which is not included in our proposed model. Although the main origin of the growth of  $I_x$  in a proposed model is a flip-flop process between a finite  $S_x$  and  $I_x$ , the cooperation of the non-collinear HFI (i.e.  $\propto I_x S_z$ ) contributes to form  $I_x$  from  $S_z$ , and may improve the qualitative agreement in relatively large  $B_x$  region. In addition, the introduction of the  $B_x$ -dependence into  $\tau_c$  and  $T_{\text{ND}}$  may improve the quantitative features.

#### IV. CONCLUSION

We investigated the in-plane nuclear field formation via Hanle effect measurements of  $X^+$  in single self-assembled InAlAs quantum dots. The observed Hanle curves showed anomalously large full width and hysteretic behavior which cannot be explained by an existing model. To reproduce the measured anomalies, we propose a phenomenological model including the nuclear quadrupolar effect and the sign inversion between in-plane and out-of-plane g-factors, which induce the compensation of  $B_x$  by  $B_{n,x}$ . The quadrupolar splitting allows a part of NSP to be preserved nearly along  $z$ -axis, which induces the  $\langle S_x \rangle$  that can change  $I_x$  via collinear HFI. The proposed model reproduces well the characteristic points of the observed anomalous Hanle curve, and consequently it has the good qualitative agreement. Therefore, we conclude that the collinear HFI is a dominant mechanism for the in-plane nu-

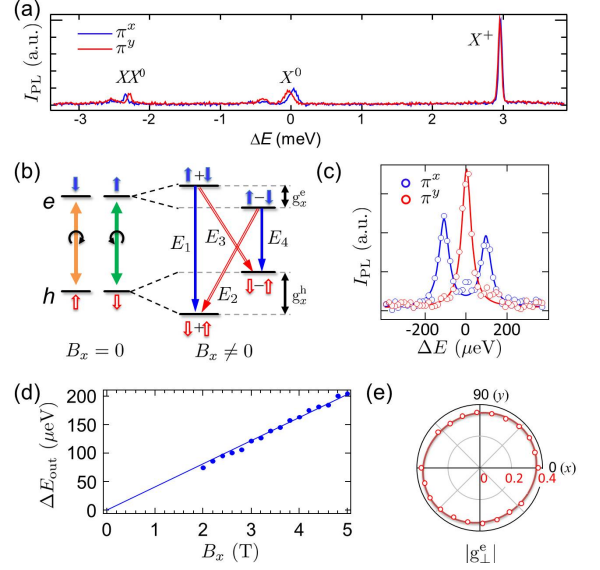


FIG. 6. (color online) (a) Polarization-resolved PL spectra of a typical SA-InAlAs QD under non-polarized excitation at 6 K and 0 T. The horizontal axis is replotted from the midpoint of the  $X^0$  doublet. (b) A level diagram of the hole (open arrows) and electron (solid arrows) states under a transverse magnetic field  $B_x$ . (c) The  $X^+$  PL spectra at  $B_x=5$  T detected in the  $(\pi^x, \pi^y)$  basis. The origin of the horizontal axis was set to the energy of the inner PL peaks. (d) The observed Zeeman splitting of the outer peaks as a function of  $B_x$ . The solid line is a fitting curve. (e) Polar plot of the magnitude of in-plane electron g-factor,  $|g_{\perp}^e|$ .

clear field formation although the non-collinear HFI may contribute to form the in-plane field in relatively large externally applied field.

#### ACKNOWLEDGMENTS

The authors would like to acknowledge H. Sasakura for sample growth and fruitful discussions. This work is supported by JSPS KAKENHI (Grants No. 26800162 and No. 17K19046) and the Asahi Glass Foundation.

#### Appendix A: in-plane electron g-factors

Here, we evaluate the in-plane electron g-factor, which is one of key parameters to describe the Hanle curves and coupled electron-nuclear spin dynamics. Figure 6(a) shows the polarization-resolved PL spectra under non-polarized excitation at 6 K and 0 T of a single InAlAs QD used in this study. The spectra indicate three emissions: the neutral biexciton ( $XX^0$ ), neutral exciton ( $X^0$ ), and positive trion ( $X^+$ ) from the low energy side. Each charge state is assigned by considering the fine structure splitting (FSS) and the binding energy. The FSS of  $\sim 73$   $\mu\text{eV}$ , the inverse pattern of FSS in the  $X^0$  and  $XX^0$  peaks, and no splitting in the  $X^+$  peak are observed clearly.

As shown in Fig. 6(b), a transverse magnetic field  $B_x$  mixes the spin-up and spin-down states for the electron of  $X^+$  and hole, respectively, and the four transitions ( $E_1$ ,  $E_2$ ,  $E_3$ ,  $E_4$ ) with linearly polarized emissions and absorptions become optically active. The Zeeman splittings of the outer peaks  $\Delta E_{\text{out}} = |E_1 - E_4|$  with  $\pi^x$ -polarization and of the inner peaks  $\Delta E_{\text{in}} = |E_2 - E_3|$  with  $\pi^y$ -polarization are given by  $\Delta E_{\text{out}} = (|g_x^e| + |g_x^h|)\mu_B B_x$  and  $\Delta E_{\text{in}} = (|g_x^e| - |g_x^h|)\mu_B B_x$ , respectively. Figure 6(c) shows the polarization-resolved  $X^+$  PL spectra at 5 T under non-polarized excitation. In this QD, there is no splitting in  $\pi^y$ -PLs within our spectral resolution, and it indicates that the magnitude of  $g_x^e$  is very close to  $g_x^h$ . Figure 6(d) shows the observed energy splitting of  $\pi^x$ -PLs in a range of 2-5 T. The observed  $\Delta E_{\text{out}}$  increases with  $B_x$ , and from the line fitting, the magnitudes of the electron and hole g-factors are deduced to be  $|g_x^e| \approx |g_x^h| = 0.35 \pm 0.01$ . Moreover, the anisotropy of the in-plane electron g-factor  $|g_{\perp}^e|$  was investigated by rotating the QD sample around  $z$ -axis. Fig. 6(e) is a polar plot of  $|g_{\perp}^e|$ , and it indicates that the in-plane g-factor anisotropy is negligible. In addition to the in-plane g-factors, the electron and hole g-factors in  $z$ -direction of this QD were evaluated independently to be  $g_z^e = -0.34 \pm 0.02$  and  $g_z^h = 2.57 \pm 0.01$  by the method canceling an optically-induced nuclear magnetic field in  $z$ -direction by a longitudinal field [22]. The obtained set of the electron g-factor, ( $g_x^e$ ,  $g_y^e$ ,  $g_z^e$ )

is used in the section of model calculations.

## Appendix B: Bloch equation

The steady state solutions of the Bloch equation (Eq. (1)) are written as

$$\langle S \rangle = \frac{S_0}{B_{1/2}^2 + (B_x + B_{n,x})^2 + B_{n,y}^2 + B_{n,z}^2} \times \begin{bmatrix} B_{1/2} B_{n,y} + B_{n,z} (B_x + B_{n,x}) \\ B_{n,y} B_{n,z} - B_{1/2} (B_x + B_{n,x}) \\ B_{1/2}^2 + B_{n,z}^2 \end{bmatrix}. \quad (\text{B1})$$

Omitting the component  $B_{n,y}$  which is very small in the simulated results, the  $x$  and  $z$  components of  $\langle S \rangle$  can be represented analytically as

$$\langle S_x \rangle = S_0 \frac{(B_x + B_{n,x}) B_{n,z}}{B_{1/2}^2 + (B_x + B_{n,x})^2 + B_{n,z}^2}, \quad (\text{B2})$$

$$\langle S_z \rangle = S_0 \frac{B_{1/2}^2 + B_{n,z}^2}{B_{1/2}^2 + (B_x + B_{n,x})^2 + B_{n,z}^2}. \quad (\text{B3})$$

where  $B_{1/2}$  ( $= \hbar/(|g_{\perp}^e| \mu_B T_s)$ ) is a half width of the normal Lorentzian curve. Eqns. (B2) and (B3) were used to obtain the expected  $\langle S_x \rangle$  and  $B_{n,x}$  from the observed  $\langle S_x \rangle$  and  $B_{n,z}$  in Fig. 5.

- 
- [1] *Optical Orientation*, Modern Problems in Condensed Matter Sciences Vol. 8, Chaps. 2 and 5, edited by F. Meier and B. Zakharchenya (North-Holland, New York, 1984).
- [2] *Spin Physics in Semiconductors*, Springer Series in Solid-State Sciences Vol. 157, Chaps. 1 and 11, edited by M. I. Dyakonov (Springer, Berlin, 2008).
- [3] Recent optical investigation of nuclear spin physics in QDs are reviewed comprehensively: B. Urbaszek, X. Marie, T. Amand, O. Krebs, P. Voisin, P. Maletinsky, A. Högele, A. Imamoglu, *Rev. Mod. Phys.* **85**, 79 (2013).
- [4] D. Gammon, Al. L. Efros, T. A. Kennedy, M. Rosen, D. S. Katzer, D. Park, S. W. Brown, V. L. Korenev, and I. A. Merkulov, *Phys. Rev. Lett.* **86**, 5176 (2001).
- [5] T. Yokoi, S. Adachi, H. Sasakura, S. Muto, H. Z. Song, T. Usuki, and S. Hirose, *Phys. Rev. B* **71**, 041307(R) (2005).
- [6] B. Eble, O. Krebs, A. Lemaître, K. Kowalik, A. Kudelski, P. Voisin, B. Urbaszek, X. Marie, and T. Amand, *Phys. Rev. B* **74**, 081306(R) (2006).
- [7] P.-F. Braun, B. Urbaszek, T. Amand, X. Marie, O. Krebs, B. Eble, A. Lemaître, and P. Voisin, *Phys. Rev. B* **74**, 245306 (2006).
- [8] A. I. Tartakovskii, T. Wright, A. Russell, A. B. Van'kov, J. Skiba-Szymanska, I. Drouzas, R. S. Kolodka, M. S. Skolnick, P. W. Fry, A. Tahraoui, H.-Y. Liu, and M. Hopkinson, *Phys. Rev. Lett.* **98**, 026806 (2007).
- [9] P. Maletinsky, C. W. Lai, A. Badolato, and A. Imamoglu, *Phys. Rev. B* **75**, 035409 (2007).
- [10] R. Kaji, S. Adachi, H. Sasakura, and S. Muto, *Phys. Rev. B* **77**, 115345 (2008).
- [11] C. P. Slichter, *Principles of Magnetic Resonance*, Chapter 10 (Springer, 1996), 3rd ed.
- [12] C. Latta, A. Högele, Y. Zhao, A. N. Vamivakas, P. Maletinsky, M. Kroner, J. Dreiser, I. Carusotto, A. Badolato, D. Schuh, W. Wegscheider, M. Atature, and A. Imamoglu, *Nat. Phys.* **5**, 758 (2009).
- [13] X. Xu, W. Yao, B. Sun, D. G. Steel, A. S. Bracker, D. Gammon, and L. J. Sham, *Nature* **459**, 1105 (2009).
- [14] A. Högele, M. Kroner, C. Latta, M. Claassen, I. Carusotto, C. Bulutay, and A. Imamoglu, *Phys. Rev. Lett.* **108**, 197403 (2012).
- [15] O. Krebs, P. Maletinsky, T. Amand, B. Urbaszek, A. Lemaître, P. Voisin, X. Marie, and A. Imamoglu, *Phys. Rev. Lett.* **104**, 056603 (2010).
- [16] E. A. Chekhovich, K. V. Kavokin, J. Puebla, A. B. Krysa, M. Hopkinson, A. D. Andreev, A. M. Sanchez, R. Beanland, M. S. Skolnick and A. I. Tartakovskii, *Nat. Nanotech.* **7**, 646 (2012).
- [17] E. A. Chekhovich, M. Hopkinson, M. S. Skolnick, and A. I. Tartakovskii, *Nat. Commun.* **6**, 6348 (2015).
- [18] R. I. Dzhioev and V. L. Korenev, *Phys. Rev. Lett.* **99**, 037401 (2007).
- [19] P. Maletinsky, doctoral thesis (Swiss Federal Institute of Technology, Zurich, 2008).
- [20] J. Nilsson, L. Bouet, A. J. Bennett, T. Amand, R. M. Stevenson, I. Farrer, D. A. Ritchie, S. Kunz, X. Marie, A. J. Shields, and B. Urbaszek, *Phys. Rev. B* **88**, 085306 (2013).
- [21] G. Sallen, S. Kunz, T. Amand, L. Bouet, T. Kuroda, T. Mano, D. Paget, O. Krebs, X. Marie, K. Sakoda, and B. Urbaszek, *Nat. Commun.* **5**, 3268 (2014).

- [22] R. Matsusaki, R. Kaji, S. Yamamoto, H. Sasakura, and S. Adachi, arXiv:1703.06046 (2017).
- [23] The width of the normal Hanle curve is determined by the spin lifetime  $T_s$  and g-factor  $g_x^e$  of a localized electron. Here,  $T_s$  and  $|g_x^e|$  are assumed to be 0.5 ns and 0.35, respectively, as typical values for single InAlAs QDs.
- [24] The following parameters are used in the calculations:  $f_e=0.015$ ,  $\tau_c=100$  ps,  $T_{ND,k}=10$  ms,  $B_Q=280$  mT,  $r_0=1.0$ , and  $\mathbf{q}$  is assumed to be along  $z$ -axis. In Fig. 4,  $g_{x(y,z)}^e=-0.35$ ,  $\tilde{A}_{x(y)}=-52.6$   $\mu\text{eV}$ ,  $\tilde{A}_z=+52.6$   $\mu\text{eV}$ ,  $g_{x(y)}^n=-0.179$ ,  $g_z^n=+0.179$ , and  $g_k^e(k=x, y, z)=-0.35$  are assumed.
- [25] The out-of-plane g-factor  $g_z^e$  of InAlAs QDs has an opposite sign of that of InAs QDs [26]. The sign of  $g_{x(y)}^e$  may be the same as that of  $g_z^e$  because of the isotropic nature of a conduction electron. In contrast, the nucleus g-factor is considered to have a large anisotropy because of QI. Considering that the anomalous Hanle curves have been observed in both kinds of SA-QDs and those facts, it is likely that the requirement of the sign inversion in the in-plane and out-of-plane of g-factors of this study could be attributed to the nucleus g-factors.
- [26] R. Kaji, T. Hozumi, Y. Hachiyama, T. Tomii, H. Sasakura, M. Jo, and S. Adachi, Appl. Phys. Express **7**, 065002 (2014).
- [27] As shown in the lower panel of Fig. 4(a), small discontinuities at  $|B_x^c|$  arise in the model calculations, while the experimental results change continuously (Fig. 5(c)). We guess tentatively that the step in Overhauser shift might be so small that we failed to detect it.
- [28] C.-W. Huang and X. Hu, Phys. Rev. B **81**, 205304 (2010).